INDEX COPERNICUS INTERNATIONAL

Bio-Algorithms and Med-Systems

WWW.BAMSJOURNAL.COM ISSN: 1896-530X

ORIGINAL ARTICLE

Received: 05.09.2025
Accepted: 30.10.2025
Published: 30.11.2025

CITE THIS ARTICLE AS:
Radler M, Moskal P, "Optimising the event selection of the total-body J-PET scanner with a brain PET insert: A simulation study," Bio-Algorithms and Med-Systems vol. 21, special issue (New Trends in Nuclear and Medical Physics), pp. 1-12, 2025, DOI: 10.5604/01.3001.0055.4540

AUTHORS' CONTRIBUTION:
A – Conceptualization
B – Data Curation
C – Formal Analysis
D – Funding Acquisition
E – Investigation
F – Methodology
G – Project Administration
H – Resources
I – Software
J – Supervision
K – Validation
L – Visualization
M – Writing – Original Draft
N – Writing – Review & Editing

CORRESPONDING AUTHOR:
Martin Rädler; Faculty of Physics, Astronomy and Applied Computer Science, Jagiellonian University; Lojasiewicza street 11, 30-348 Kraków, Poland;
E-mail: martin.raedler@uj.edu.pl

Optimising the event selection of the total-body J-PET scanner with a brain PET insert: A simulation study

Martin Rädler[1,2ABCEFIKLMN], Paweł Moskal[1,2ADFGHJN] for the J-PET collaboration

[1]Faculty of Physics, Astronomy and Applied Computer Science, Jagiellonian University, Kraków, Poland
[2]Center for Theranostics, Jagiellonian University, Kraków, Poland

ABSTRACT

Objective: Positron emission tomography (PET) scanners with plastic scintillators offer more cost-effective instrumentation to image the distribution of radiopharmaceuticals. However, inter-detector scatters among plastic scintillators can lead to more false coincidences than in conventional PET scanners, since annihilation photons in plastic scintillators dominantly interact via Compton scattering, which deposits only a portion of the photon energy. A scatter test (ST), combined with a lower energy deposition threshold of 200 keV, has been used to preselect the coincidence events.

Methods: In this work, we investigate the impact of temporal and spatial resolution limitations as well as a variation of the energy threshold on the preselection and different subsequent coincidence event selection policies via Monte Carlo simulations. We simulate the total-body Jagiellonian-PET (TB-J-PET), combined with a brain PET insert imaging a human-sized water phantom.

Results: We find that coincidence time resolution (CTR) worse than 200 ps poses limitations on the ST for scanners close to the patient, such as the brain PET. Also, coincidence event selection requiring energy loss higher than 200 keV performs sub-optimally, whereas a lower energy threshold (50 keV), combined with a time-based selection policy, can capture a higher percentage of true events, even under realistic time resolution.

Conclusions: We recommend the adaptation of a time-based event selection policy together with a lowered energy threshold, which can also significantly increase sensitivity, as the latter rises faster than the fraction of true and non-phantom--scattered events decreases. Dedicated analyses in the scatter-corrected image domain are necessary to further investigate this potential.

KEYWORDS

J-PET, total body PET, brain PET, plastic scintillators, event selection

LIST OF ABBREVIATIONS

BGO – bismuth germanium oxide
CDF – cumulative distribution function
CTR – coincidence time resolution
FOV – field-of-view
FWHM – full width at half maximum
GATE – Geant4 application for tomographic emission
J-PET – Jagiellonian positron emission tomography
LOR – line of response
LSO – lutetium oxyorthosilicate
MC – Monte Carlo
SiPMs – Silicon PhotoMultipliers
ST – scatter test
STR – single time resolution
TB-J-PET – total body J-PET
WLS – wavelength-shifting

INTRODUCTION

The J-PET collaboration (Jagiellonian positron emission tomography) is working towards the realisation of a large field-of-view (FOV) total body J-PET (TB-J-PET) scanner [1–4]. TB-J-PET, similarly as current clinical total-body PET scanners [5–9], will provide, among other things, low-dose imaging, short scan times, and dynamic imaging. In addition, it will also enable total-body positronium imaging [10, 11] and total-body quantum entanglement imaging [12, 13]. The key distinctive feature, i.e., the utilisation of cost-effective plastic scintillators over conventional crystals, such as bismuth germanium oxide (BGO) or lutetium oxyorthosilicate (LSO), could facilitate a wider adoption of large FOV scanners [1]. The TB-J-PET follows the development of a prototype scanner built from plastic scintillator strips read by vacuum tube photomultipliers [14–16] and a portable modular scanner read by Silicon PhotoMultipliers (SiPMs) [11, 17, 18].

Simultaneously, the molecular insights provided by specific radiotracers have motivated the development of dedicated brain PET scanners. Maps of serotonin [19] or kappa receptors [20], kinetic modeling [21], and the diagnosis of neurological diseases, such as dementia [22] or cancer [23], are some of the applications for brain PET scanners. Various scanner geometries have been proposed and developed, ranging from the conventional cylindrical shape to more exotic helmets with horizontal or seated patient positioning [24–34]. Comprehensive overviews of brain PET scanners are also available in the literature [35–38]. In ongoing studies [39], we are characterising the sensitivity as well as the spatial resolution of the TB-J-PET, *combined* with a brain PET insert also built from plastic scintillators.

In this work, we investigate realistic coincidence event selection, taking into account temporal and spatial resolution limitations. Whenever multiple hits (detected interactions of single photons with the scanner) occur within a coincidence window, *coincidence event selection* – or simply *event selection* – determines which coincidence is chosen. We aim to bridge the gap between the processing and analysis of Monte Carlo (MC) simulated data and experimental data by exploiting the same techniques routinely used for the latter [11]. This study is primarily aimed at the TB-J-PET combined with a brain PET insert, yet our conclusions and proposed event selection approach can also be applied only to the TB-J-PET and other plastic scintillator-based scanners. The primary parameters under investigation are the energy window (particularly the lower energy threshold) and the coincidence time resolution (CTR).

Regarding the energy window, hits are only considered if they deposit an amount of energy that lies within a certain energy range. For conventional crystal PET scanners that can absorb the annihilation photons entirely through, e.g., the photoelectric effect, the energy window is chosen to be narrow (some tens of keVs) around the 511 keV photopeak, with some variability between different vendors [7, 40–43]. Occasionally, variations of the energy window are investigated [44, 45]. For plastic scintillators, however, a selection around a simple photopeak is not possible due to the broad energy deposition spectrum of Compton scattering, as described by the Klein–Nishina formula. The largest possible energy deposition is given by the Compton edge, at $\frac{2}{3}$ 511 keV ≈ 341 keV. An upper energy threshold is thus not usually set, unless high-energy photons (prompt gammas) are involved [46]. Previous studies settled on the lower energy threshold of 200 keV [2, 4, 47–50], aiming to reduce noise due to scattering within the patient's body and the detector. In this work, we systematically investigate a variation of the lower energy threshold and its impact on scatter fraction as well as sensitivity.

Finally, in contrast to a more conventional energy-based event selection, we propose a time-based event selection, potentially leveraging the excellent time resolution potential of plastic scintillators [51]. For this purpose, we considered a range of CTRs up to 600 ps (guided by experimental limitations [52]) and analysed as well as compared the efficiencies of different policies.

MATERIALS AND METHODS

The following section describes the conducted MC simulations and subsequent data analysis.

Monte Carlo simulation

MC simulations were conducted via the Geant4 application for tomographic emission (GATE) [53–57]. We used version v9.4, which enables the simulation of multidetector geometries and draws coincidences between them (available since v9.3 [58]). In addition, we patched v9.4 in three places to resolve some issues. Details are described in *Appendix A*.

The geometry under investigation is depicted in Fig. 1. The dimensions of the TB-J-PET were taken from the latest design, comprising two rings of 33-cm axial length and three rings of 60 cm [59]. The distance between the two TB-J-PET scanners was 2 cm, equal to the spacing between the rings. The brain insert features smaller scintillators for increased spatial resolution. In particular, they were narrower (4 mm instead of 6 mm) and had a smaller depth (18 mm instead of 30 mm). Detailed dimensions are listed in Tab. I.

We simulated a water phantom comprising two cylinders. One represents a human body (from the neck down) with a length of 1.51 m and a diameter of 40 cm. The other represents a human head with a diameter of 20 cm and the same length as the brain insert, i.e., 33 cm. The chosen dimensions are roughly guided by median human measures, though generously rounded. Data from the ANSUR II study [61] provides median human measures (female/male [mm]). From the head breadth (147/154) and head length (190/200) we chose the 200-mm head cylinder diameter. From the bi-deltoid breadth (450/509) and hip breadth (353/344), we chose the body cylinder diameter of 400 mm. The difference between the stature and the acromial height (293/315) justifies the head cylinder length of 330 mm. Only the acromial height (1332/1439) slightly deviates from the chosen body cylinder height of 1510 mm, which was chosen based on symmetry, i.e., the distance between the phantom edge and the TB-J-PET edge is equal on both sides. We simulated an overall activity of 1 MBq for the entire phantom to reduce the number of random events. We ran the simulation for 100 s, which we deem sufficient statistics.

Tab. I. Geometric parameters of the scanners depicted in Fig. 1. Wavelength shifters (WLSes) were used to enhance the axial resolution [60].

PARAMETER [UNIT]	TB-J-PET UPPER BODY	TB-J-PET LOWER BODY	BRAIN INSERT
Scanner			
Radius [mm]	446.6	448.1	164.6
Axial length [mm]	680	1840	330
Axial offset [mm]	930	–350	755
Ring length [mm]	330	600	330
Gap between rings [mm]	20	20	–
Number of rings	2	3	1
Number of modules	24	24	12
Within each module: active layers			
Number of layers	2	2	2
Radial offset [mm]	± 16.8	± 18.3	± 11.3
Transaxial repetitions	16	16	16
Transaxial spacing [mm]	0.6	0.6	0.6
Each scintillator			
Radial size (depth) [mm]	30	30	18
Trans-axial size (width) [mm]	6	6	4
Axial size (length) [mm]	330	600	330
Within each module: WLSes			
Number of layers	1	1	1
Radial offset [mm]	0	0	0
Axial repetitions	50	90	75
Axial spacing [mm]	0.4	0.4	0.4
Each WLS			
Radial size (depth) [mm]	3	6	4
Trans-axial size (width) [mm]	108	108	75
Axial size (length) [mm]	6	6	4

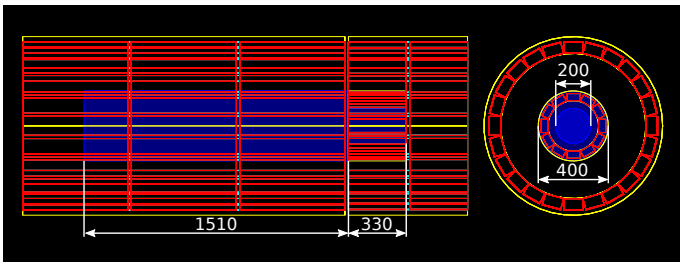

Fig. 1. PET scanner geometry and phantom simulated with GATE.

We assigned an activity of 948,195 Bq to the body cylinder and 51,805 Bq to the brain cylinder, which corresponds to equal activity concentration. We simulated isotopically distributed back-to-back events with monoenergetic energies of 511 keV.

For the digitiser, we decreased the lower energy threshold from the usual 200 keV to 50 keV, keeping the energy resolution of 23% at the reference energy of 200 keV. Note that "Hits" in experimental J-PET studies corresponds to `Singles` [62] in the GATE naming convention. We do not refer to the `Hits` in GATE. We introduced time resolution on the `Singles` via Gaussian blurring. The relation between the single time resolution (STR) and the CTR is given as CTR = $\sqrt{(2\,\mathrm{STR}^2 + \mathrm{S}^2)}$, where S indicates geometry-related time spread due to depth-of-interaction. Without explicit modeling of the latter, CTR = $\sqrt{2}$ STR. To simulate CTRs of 0, 200, 400 and 600 ps, we set the full width at half maximum (FWHM) of the `Singles` to 0, 200/$\sqrt{2}$, 400/$\sqrt{2}$, and 600/$\sqrt{2}$ ps. We only exported coincidences but removed any further filtering from GATE by choosing the policy `takeAllGoods`. Consequently, `Singles` can be used multiple times in different coincidence entries. We applied a coincidence window of 4 ns, which were simultaneously and individually opened for each single event (GATE setting: `allDigiOpenCoincGate true`).

We ran a total of eight different simulations: four each with and without the phantom for the four different CTRs. All simulations used the same phantom-sized source.

Data analysis

The flowchart of our data analysis is shown in Fig. 2. The "Exported raw GATE coincidences" were stored in the `.root` output files from GATE. Any further processing was carried out via Python.

The first step, i.e., to "remove coincidences in neighboring sectors" does in principle the same as `minSectorDifference` [62] from GATE, making sure not to remove coincidences with close `rsectorID`'s that are in different scanners (see *Appendix A*). In particular, we set a minimum sector difference of two, i.e., coincidences cannot occur in the same or nearest neighboring sectors but are allowed in the next to nearest neighbor sectors and onwards.

In the next step, we conducted a *Scatter Test* (ST), which aims to check and exclude coincidences that are light-like and thus likely

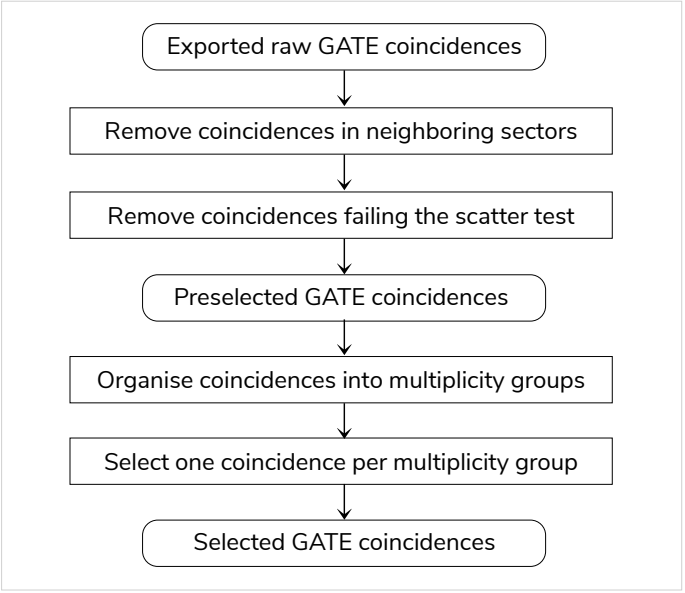

Fig. 2. Flowchart of our data analysis.

caused by one photon. In that case, the quantity ST ≡ $|\mathbf{r}_2 - \mathbf{r}_1| - (t_2 - t_1)c_0$ vanishes, where $\mathbf{r}_1$ & $\mathbf{r}_2$ and t_1 & t_2 are the interaction positions and the times of the two coinciding events, respectively, and c_0 is the speed of light. Due to the inherent time sorting of GATE, $t_2 - t_1 \geq 0$. For true events ST $\gtrsim$ 0, whereas false coincidences have ST $\lesssim$ 0. ST is subject to spatial and temporal resolution. For the former, instead of using the exact interaction positions, we used the radial and trans-axial scintillator centres. Since the axial position is reconstructed in J-PET detectors [15, 60], we added an axial uncertainty with a FWHM equal to the WLS dimensions (see Tab. I.). At the scintillator edges, the blurring was done according to a truncated normal distribution.

We referred to the coincidences remaining after the first two steps as the "preselected GATE coincidences". From them, we obtained the multiplicity. For this purpose, we looped through the list of coincidences and grouped them, if they have shared `Singles`. For instance, consider four coinciding `Singles` at sorted times t_0, t_1, t_2, and t_3 such that $t_3 - t_0 < 4$ ns (all within one coincidence window). For this case, where the multiplicity m is equal to four, GATE can draw at most $m(m-1)/2 = 6$ coincidences. Consequently, we group these at most six coincidences together and assign them a multiplicity of four. The time sorting within the group (which will be more important for the event selection policies described below) is in our example as follows:

Coincidence number	1	2	3	4	5	6
Single event index 1	0	0	0	1	1	2
Single event index 2	1	2	3	2	3	3

The final step was the event selection using different policies. Our guiding principle was to choose exactly one event per multiplicity group. In this work, we studied the following four event selection policies:

- **Ideal:** Choose all true coincidences within each multiplicity group; if no true coincidences are present, choose the first in the group.
- **Time-based: selection → threshold (sel. → thresh.).** Choose the first coincidence of each multiplicity group from the complete dataset and the threshold based on energy.
- **Time-based: threshold → selection (thresh. → sel.).** Choose the first coincidence of each multiplicity group from dataset that remains after applying the energy threshold.
- **Energy-based:** Choose the coincidence with the highest total energy deposited ($E_1 + E_2$).

The ideal policy will not be 100% true, since there are multiplicity groups that have no true coincidences among them. Furthermore, the difference between the two time-based approaches is that the event selection is made given different amounts of data. The *time-based sel. → thresh.* – approach chooses the coincidences once with the data reached a threshold of 50 keV and progressively excludes them when the energy threshold is raised. The *time-based thresh. → sel.* – approach make its choice dependent on the data that is left at the given energy threshold. Finally, there are different energy-based event selection polices possible besides the one listed above. For instance, one could always choose the coincidence that involves the event with the highest energy deposition paired with the event that deposited the highest amount of energy among its possible partners. For example, say one multiplicity group features a coincidence with $E_{a,1}$ = 270 keV and $E_{a,2}$ = 100 keV, as well as a coincidence of $E_{b,1}$ = 200 keV and $E_{b,2}$ = 180 keV. While $E_{b,1} + E_{b,2}$ is larger, it does not feature the event with the largest energy deposition of $E_{a,1}$. We also implemented this alternative energy-based coincidence selection policy and found that there is practically no difference in the chosen energy-based policy.

We analysed the quality of the different event selection polices by the percentage of true coincidences chosen. For the simulations without the phantom, a true coincidence originated from the same annihilation (`eventID1 = eventID2` [62]), underwent zero Rayleigh scatterings in the detector (`RayleighCrystal1 = RayleighCrystal2 = 0`) and exactly one Compton scatter (`comptonCrystal1 = comptonCrystal2 = 1`) for each of the two `Singles` (The present utilisation of the Compton and Rayleigh counts underlines the importance of the last patch described in *Appendix A.*). For the simulations that include the water phantom, we distinguish between *true in detector*, which corresponds to the previous one, and *true in phantom*, which means that none of the two photons involved scattered in the phantom.

In particular, both `comptonPhantom1 = comptonPhantom2 = 0` and `RayleighPhantom1 = RayleighPhantom2 = 0` are necessary for the latter. When referring to just *true coincidences* for the simulation with the phantom, they must be both true in the detector as well as in the phantom.

Finally, we assessed the error of phantom scattered coincidences via the minimum distance between the source point $\mathbf{p}_s$ and the line of response (LOR) passing through the points $\mathbf{p}_1$ and $\mathbf{p}_2$:

$$d_{min} = |(\mathbf{p}_s - \mathbf{p}_1) \times (\mathbf{p}_2 - \mathbf{p}_1)| \,/\, |\mathbf{p}_2 - \mathbf{p}_1|, \qquad (1)$$

where $\mathbf{p}_1$ and $\mathbf{p}_2$ are the exact interaction positions (`globalPos <X, Y, Z><1, 2>` [62]) such that true coincidences have a vanishing d_{min}. This analysis was only conducted for non-random coincidences, i.e., those that have a common $\mathbf{p}_s$.

RESULTS

The order of results presented in this section follows the one outlined in Fig. 2. Recall that simulations *without phantom* refer to simulations that do not feature the water phantom. Nevertheless, the same-sized uniform back-to-back annihilation photon source is still present.

Preselection

The results of the first two steps of Fig. 2. are shown here. With a minimum sector difference of two, about 45% of the coincidences of the data without the phantom and about 54% of the data with the phantom were rejected. Naturally, the latter did not depend on time resolution. The distribution of the ST of the remaining coincidences without and with the phantom are shown in Fig. 3. and 4. A natural lower threshold on the ST (excluding events below the threshold) would be to choose the first minimum after the main peak at zero. The thresholds are indicated by black vertical lines. However, due to the increasing overlap between the scattered and true events, we set a maximum threshold value of 10 cm on the ST. This primarily affected simulations with a CTR larger than 200 ps. The percentages of the coincidences that passed the scatter test are listed in Tab. II.

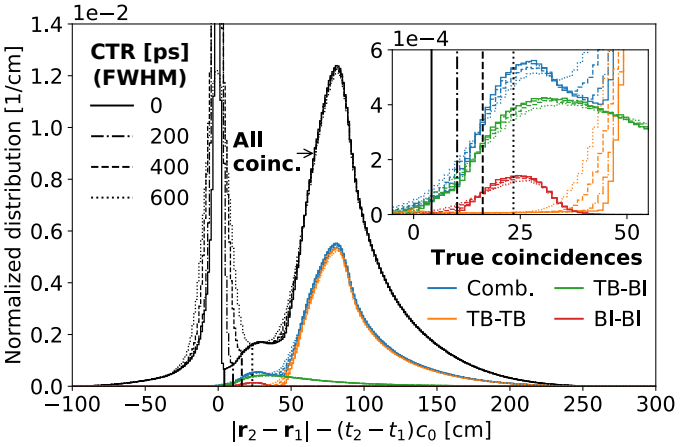

Fig. 3. Distribution of the scatter test without the phantom for different CTRs. The colored true coincidences are divided into the combination of both scanners (Comb.), both events in the TB-J-PET (TB-TB), one in the TB-J-PET and brain insert each (TB-BI), and both in the brain insert (BI-BI). All histograms of a given time resolution are normalised with respect to integral along the ST of all coincidences (black). The insert shows a closeup focused on the data that involves the brain insert.

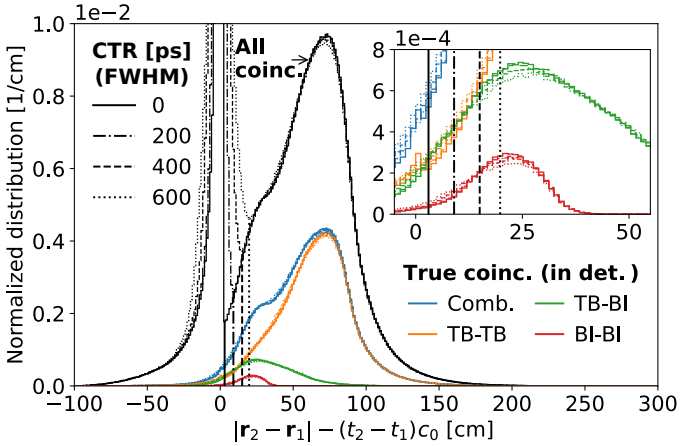

Fig. 4. Distribution of the scatter test with the phantom for different CTRs. Details as in the caption of Fig. 3. Recall that **True coincidences (in detector)** means that the coincidences still might have undergone phantom scatters.

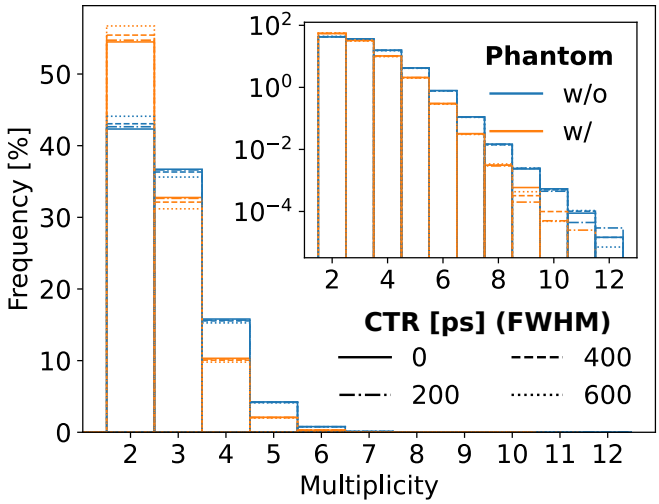

Fig. 5. Multiplicity distribution for different time resolutions with (w/) and without (w/o) phantom. The insert shows the same data logarithmically scaled.

Coincidence selection: performance analysis

As outlined in Fig. 2., we first need to organise the data into multiplicity groups before the coincidence selection. The distribution of the multiplicity is shown in Fig. 5.

Fig. 6. presents the performance analysis in terms of the percentage of true coincidences for the different policies and time resolutions, together with an estimate of sensitivity for the simulations without the phantom. The equivalent results from the simulations that involve the phantom are shown in Fig. 7. There we also added the percentage of non-phantom-scattered coincidences. In addition, since a non-negligible portion of photons undergoes very minor phantom scattering, we also added a more tolerant estimation of non-phantom-scattered coincidences. If the LOR passes close to the

Tab. II. Percentage of events passing the scatter test. The threshold is chosen to be at the first minimum after zero, yet no larger than 10 cm.

CTR [ps]	0	200	400	600
Without phantom [%]	73.1	72.7	73.2	74.6
With phantom [%]	64.9	63.4	63.7	65.4

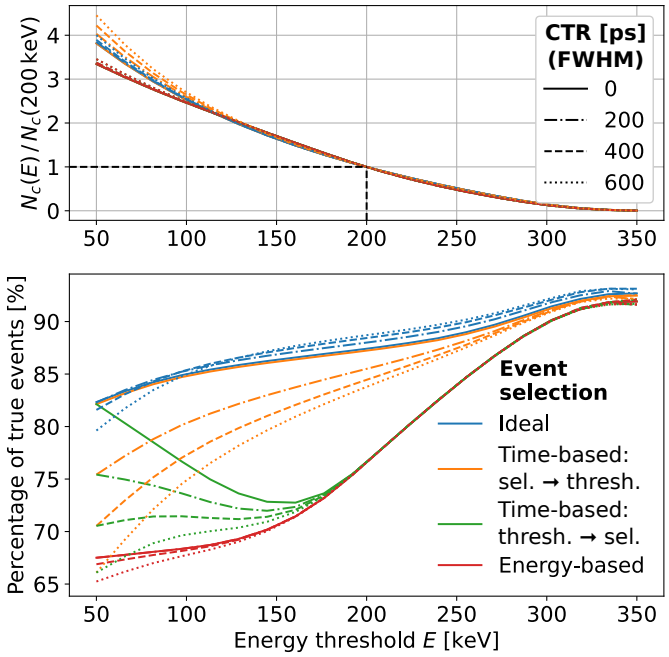

Fig. 6. Sensitivity and efficiency of different coincidence selection policies as a function of the time resolution as well as the energy threshold in the scenario without the scattering phantom. In the upper panel, N_c indicates the number of coincidences. The data is normalised to the value of N_c at 200 keV.

common annihilation point with a tolerance of $d_{min} \leq 3$ mm (based on the order of the expected spatial resolution), it is still considered non-phantom scattered. This tolerance is added since an experimental scatter fraction measurement would not be able to distinguish small-angle phantom scatters from non-scattered coincidences.

Coincidence selection: error analysis

In addition to quantifying the efficiency via the percentage of true coincidences, we also studied the error of the incorrectly identified coincidences via d_{min}, as defined in Eq. (1). The d_{min} distributions are shown in Fig. 8. for the ideal time resolution case. We focus on $d_{min} \geq 10^{-4}$ mm (only the erroneous ones) and show their median for all policies and time resolutions in Fig. 9. as a function of the energy threshold.

Finally, we also investigated the amount of error introduced by phantom-scattered events.

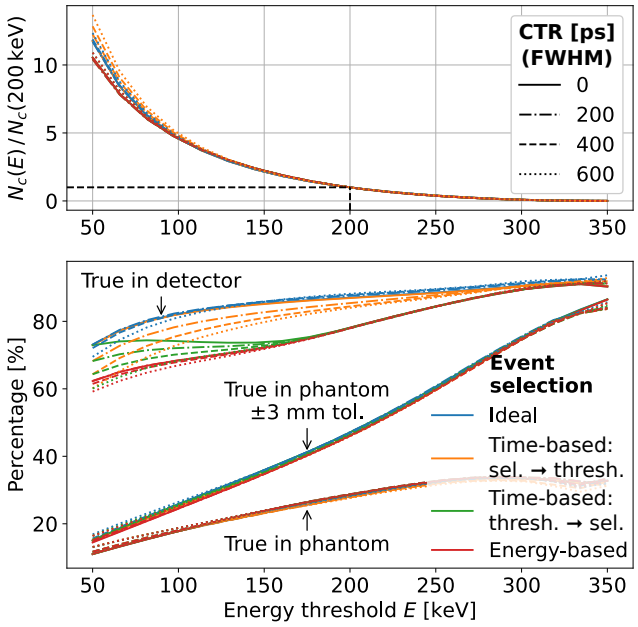

Fig. 7. Same as Fig. 6. with the phantom. "True in phantom" refers to the non-phantom-scattered coincidences. Details of the tolerant estimate are in the text.

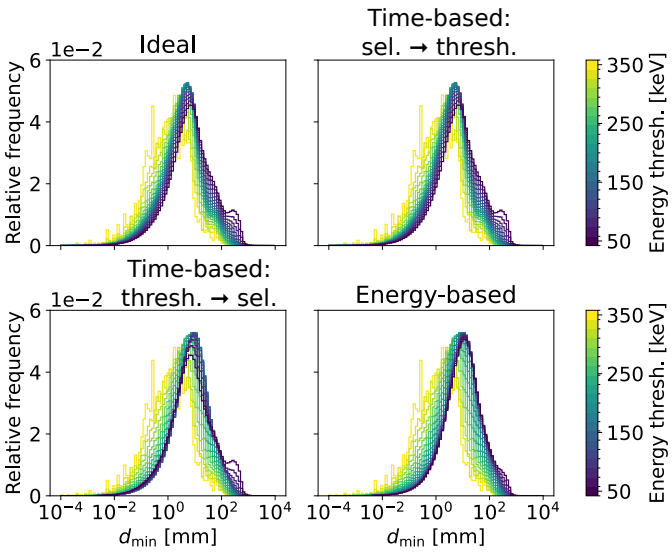

Fig. 8. Distributions of d_{min} as defined in Eq. (1) for the different coincidence selection policies for the ideal time resolution of (CTR = 0 ps), using the simulation without the phantom.

Therefore, we conducted the same analysis as shown in Fig. 8., with the data from the simulations that involve the water phantom and filter for the phantom-scattered coincidences (Fig. 10., 11.).

DISCUSSION

The ST is an important event selection tool, especially for PET detectors built from plastic scintillators that suffer from a significant

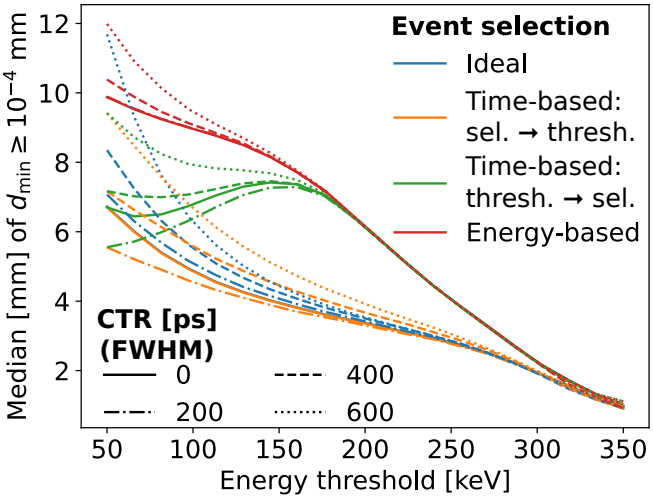

Fig. 9. Median of the distributions shown in Fig. 8. for all time resolutions under investigation.

amount of detector scatters. However, with the distribution of the ST shown in Fig. 3. and 4., we have pointed out its limitations for geometries that involve brain PET scanners with realistic time resolution. In particular, in Fig. 3. and 4. we see how the sharp peak of scattered events at ST = 0 gradually widens with worsening CTR. Thereby, the scattered coincidences spill into the domain of true events, as shown with the colored distributions. Excluding the majority of the scattered events by setting the threshold at the first minimum after the main peak (black vertical lines), which move out with increasing CTR, would also cut true events from the brain PET insert. In particular, at a CTR of 600 ps, about half of the BI-BI coincidences would be systematically removed, i.e., primarily affecting the coincidences from the outer edge of the phantom. The reason for this is that the brain PET scanner is significantly closer to the phantom than the TB-J-PET, such that true and scattered events can become indistinguishable. To avoid this issue, a maximum ST threshold value of 10 cm was chosen, which primarily affected the data from time resolutions above 200 ps. Generally, the maximum threshold value should be guided by the distance between the diameter of the scanner and the diameter of the imaged object (compare the brain insert parameters from Tab. I. to the phantom parameters shown in Fig. 1.). One could also choose a separate ST threshold for the TB-J-PET. Notice how the difference between the TB-J-PET ring diameter and the body phantom diameter is roughly equal to the ST value, where the distribution of true TB-TB coincidences rises (at about 45 cm). The impact of keeping the ST threshold below 10 cm is also shown in Tab. II. The ST passing percentage first decreases from 0 ps to 200 ps CTR, due to the moving threshold and an overlap with the events situated between roughly 0 and 10 cm. However, from 400 ps onward, the passing rate increases due to the fixed threshold and scattered events spilling beyond 10 cm. In this scenario, we are forced to accept more scattered events, which need to be filtered out in a later stage.

The distribution of the multiplicity determined after the preselection was shown in Fig. 5. Recall that we only exported coincidence

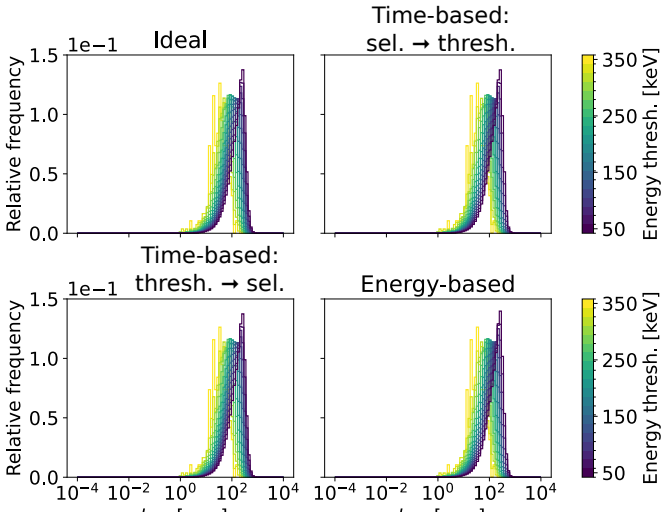

Fig. 10. Distributions of d_{min} as defined in Eq. (1) for the different coincidence selection policies for the ideal time resolution of (CTR = 0 ps), using the simulation with the phantom, filtered for phantom-scattered events.

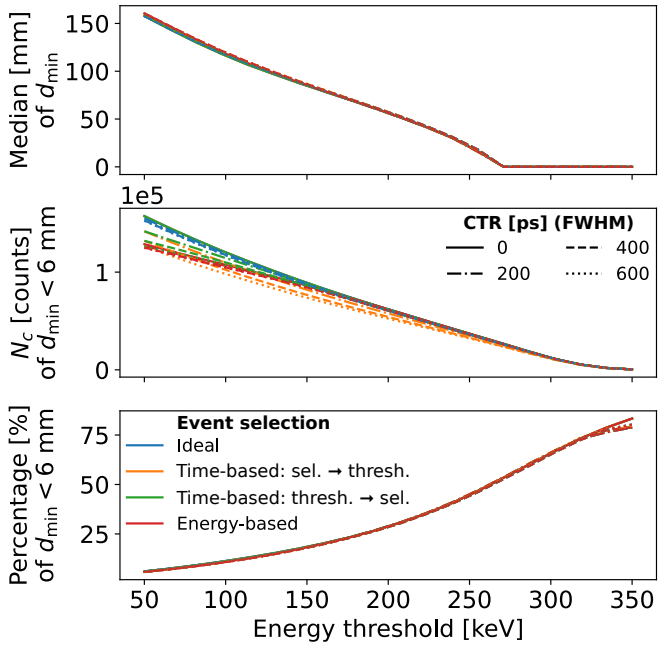

Fig. 11. Analysis of the distributions shown in Fig. 10. for all time resolutions under investigation.

events so that there was no multiplicity of one. This approach is significantly more efficient in terms of data storage and memory, since a large fraction of the data usually constitutes the superfluous multiplicity one events. This is also advantageous, considering that more data needs to be stored when lowering the energy threshold to 50 keV. Generally, the distributions shown in Fig. 5. approximately follow the exponential falloff. However, the multiplicity shown in this work initially decreases less rapidly than in, e.g., [11] (counts usually drop by about a factor of five between successive multiplicities), likely due to the different scanner geometry, i.e., using two-layer versus one-layer. At higher multiplicities the decline is steeper than in [11], since experimental data has a background of cosmic radiation, which is more prominent at higher multiplicities. Furthermore, time resolution has naturally little to no impact on the shape of the distribution. The simulations that involve the water phantom have a tendency towards lower multiplicity due to the photons that are absorbed in the phantom.

The key outcomes of this work are shown in Fig. 6. and 7. The rising number of coincidences, as shown in the upper panels, depends only very weakly on the CTR and coincidence selection policy. However, a significant difference is between the simulation without and with the water phantom. For the latter, $N_c(E)$ rises faster when the energy threshold is lowered. This effect can primarily be attributed to phantom scattering, which effectively lowers the energy of the annihilation photons (and changes their path) so that more events can be found at lower energies. This is also reflected in the decreasing fraction of non-phantom scattered events, as shown in the bottom panel of Fig. 7. Generally, increasing sensitivity provides an incentive to lower the energy threshold. For the data without the scattering phantom, compare $N_c(E)$/N_c(200 keV) to the percentage of true events for the ideal event selection. For example, at a threshold of 100 keV, the sensitivity has more than doubled (compared to the case where the threshold is at 200 keV), while the percentage of true coincidences drops by only a couple of percent. (In other words, the blue lines in the bottom panel of Fig. 6. are relatively flat). Nevertheless, for the more realistic scenario that involves a phantom, we also need to take the percentage of scattered coincidences into account. Unfavorably, the fraction of non-phantom-scattered coincidences decreases for lower energy thresholds, even more so for the more tolerant estimate (see the bottom panel of Fig. 7.). However, this needs to be contrasted with the rise in sensitivity. Consider the same example as before. At 100 keV the sensitivity has roughly increased fivefold, whereas the fraction of non-phantom-scattered coincidences decreases by less than half. Whether lowering the energy threshold in order to increase sensitivity does more harm than good due to increased phantom scattering needs to be investigated further. Analyses of image reconstructions with different data sets using different energy thresholds are necessary. Also, dedicated energy-threshold-dependent scatter correction would be needed. Both are beyond the scope of this work.

We continue with the performance of different coincidence selection strategies shown in the bottom panel of Fig. 6. The following holds also for "true in detector" from the bottom panel of Fig. 7. Firstly, the graphs for *time-based: sel. → thresh.* and *time-based: thresh. → sel.* for each CTR meet at 50 keV, as expected, and are thus consistent with their respective definitions. What is remarkable is that under ideal time resolution, the *time-based: sel. → thresh.* – approach performs almost optimally, i.e., the solid blue and orange curves are practically overlapping.

Naturally, the performance of *time-based: sel.* → *thresh.* decreases with worsening CTR, as the correct first event can no longer be assessed accurately. Nonetheless, the performance of *time-based: sel.* → *thresh.*, even for a CTR of 600 ps, is better than the time--based approach with limited data (*time-based: thresh.* → *sel.*) and the energy-based approach. Specifically, considering an optimistic CTR of 200 ps and maintaining an energy threshold at 200 keV to keep the number of scatters low, we find that the *time-based: sel.* → *thresh.* policy performs about 10 percent better than the energy-based approach. Moreover, notice how *time-based: thresh.* → *sel.* and the energy-based policies behave almost identically above 200 keV. The reason for this is twofold. Firstly, both policies do not take the information from lower energy events into account. Secondly, due to the nature of Compton scattering, it impossible for an annihilation photon with 511 keV to deposit more than 200 keV twice. In fact, the highest possible energy a single 511 keV photon can deposit twice via Compton scattering is equal to $(7 - \sqrt{17})/8\ m_e c^2 \approx 184$ keV. (This also motivated the reference value of 200 keV in an effort to reduce detector scatters). Consequently, *time-based: thresh.* → *sel.* and energy-based policies are equal above 184 keV, since there are not many coincidences to choose from in each multiplicity group in the first place. At this stage it is more relevant to know which events to discard and which are done with *time-based: sel.* → *thresh.* by taking low-energy scattering into account. Therefore, a time-based coincidence policy is only beneficial if low-energy events are not discarded.

In Fig. 8. and 9. we have analysed the incorrectly attributed coincidences, ranging from 35 to 5% of the data, depending on event selection policy and CTR. The statistics of this analysis vary significantly, following $N_c(E)$ from Fig. 6. Consequently, the histograms at the higher energy thresholds show more statistical variations. We have chosen to study d_{min} as a simple tool to assess the error. However, this analysis does not take time of flight (TOF) into account. d_{min} might be small if the actual and assumed source points are both on the LOR. The latter could be resolved with TOF information. We assume this to be rather infrequent, yet acknowledge that this analysis could be improved in future work.

The distributions of the deviation d_{min} in Fig. 8. are generally widespread, ranging from sub-millimeters to meters. Since higher energy interactions lead to larger angle scattering, one can observe a trend towards larger d_{min} when lowering the energy threshold. A more insightful analysis of this data is given in Fig. 9. The cutoff at 10^{-4} mm was chosen based on the smooth falloff of the distributions from Fig. 8. Some true events have non-zero $d_{min} < 10^{-4}$ mm due to numerical instabilities when evaluating Eq. (1). We have verified that the cumulative distribution function (CDF) at this threshold follows the graph of Fig. 6., confirming that $d_{min} < 10^{-4}$ mm are true events.

In Fig. 9. we see the same general trend as in Fig. 8., i.e., larger deviations towards lower energies. What is interesting, however, is that not only do the *time-based: thresh.* → *sel.* and the energy--based polices have a higher fraction of misclassified coincidences (as shown in Fig. 6.), but also the misclassified events have a larger median deviation by up to 3 mm. Moreover, while we could see a clear decrease in the percentage of true events with worsening CTR (*time-based: sel.* → *thresh.* in Fig. 6.), we do not see significant differences of the median d_{min}. In fact, all CTRs are close to the *ideal* standards.

Finally, we ran a similar analysis for the scattered events (see Fig. 10. and 11.). Differences between different policies and CTRs are small, so we focus only on the general trend. As seen in the upper panel of Fig. 11., the lower the energy threshold, the larger phantom-scatter-related errors, which is consistent with expectations. In the following, we have chosen a cutoff value of 6 mm. This value is related to the ± 3 mm tolerance we showed in Fig. 7., where we assumed that one could not experimentally differentiate between true and small scatter events. In that order of magnitude, we assumed the spatial resolution of the scanner. We assume the scattered events with deviations below 6 mm to be most detrimental to spatial resolution, causing blurring in the immediate vicinity of an active region. In the middle panel of Fig. 11. we see that the absolute number of such close scatters increases with a lower energy threshold. However, the relative number shown in the panel below decreases, meaning that their contribution diminishes statistically. However, as mentioned previously, this aspect needs to be investigated in a separate work, involving dedicated phantoms and scatter correction algorithms. Finally, recall that we ran our simulations at a relatively low activity of 1 MBq to suppress random coincidences. Although appropriate for this proof-of-principle study, future work should also examine higher and more clinically relevant activities.

CONCLUSIONS

In this work we have used MC simulations to investigate the impact of temporal and spatial resolution limitations on preselection and different event selection policies for a combined TB-J-PET and brain PET insert scanner. Firstly, we have pointed out that a CTR worse than 200 ps poses limitations to the scatter test. In particular, with the brain PET insert being significantly closer to the patient, true and scattered events become increasingly indistinguishable with poorer CTR. In order not to systematically remove brain PET events, one must tolerate a larger scattering background. Secondly, we find that the usual lower energy threshold of 200 keV together with a conventional energy-based event selection policy performs sub-optimally. On the contrary, a time-based policy, together with an energy threshold down to 50 keV, performs almost ideally under ideal CTR, and still better than an energy-based approach, even under worse CTR. Also, the error of the false coincidences, as quantified via the minimum distance between the source point and the LOR, is lower with the time-based policy. Thereby, one can potentially leverage the excellent time resolution potential of plastic scintillators. Generally, a significant increase in sensitivity could be achieved by lowering the energy threshold. Both the fraction of true events as well as the fraction of non-phantom scattered

events decrease less than the sensitivity rises with a lower energy threshold. Previous concerns regarding scattering need to be reconsidered and properly evaluated in the image domain. Even if coincidences below 200 keV are eventually not used for the image reconstruction, they should be kept to enable a time-based coincidence selection policy. Note that low energy events are kept in experiments with J-PET detectors, so our approach can easily be adapted to experimental data. However, more data needs to be processed for this event selection approach, which raises computational demands.

APPENDIX A: GATE 9.4 PATCHES

Here we describe the changes in the GATE v9.4 source code used in this study. They were also presented in [63]. Identical changes would also be necessary for v9.3. Firstly, our geometry consists of multiple `cylindricalPET`'s [62]. For each such geometrical object instantiated, GATE creates a separate `CoincidenceSorter` called "Coincidences". This leads to ambiguity when activating the export of coincidences. To fix that, we removed the automatically generated `CoincidenceSorter` and initiated a dedicated one separately.

Secondly, the parameter `minSectorDifference`, aimed to remove coincidences from neighboring or close detector sectors, does not distinguish between different scanners (different `cylindricalPET`'s). It removes coincidences with the same `rsectorID` even if they occurred in different scanners. Therefore, we set the `minSectorDifference` to zero (which requires a minor patch, since its minimal value is one) and removed neighboring coincidences in post-processing. Finally, v9.3 GATE processes the hits layer by layer independently, so that the counter of Compton or Rayleigh interactions does not account for interactions in different layers and generally underestimates the counts. We patched the issue and ensured consistency with the previous GATE version v9.2. Our code is available upon request.

ACKNOWLEDGMENTS

We acknowledge support from the National Science Centre of Poland through grant no. 2021/42/A/ST2/00423, the SciMat and qLife Priority Research Areas budget under the program Excellence Initiative – Research University at Jagiellonian University, and we also acknowledge the Polish high-performance computing infrastructure PLGrid (HPC Center: ACK Cyfronet AGH) for providing computer facilities and support within computational grant no. PLG/2024/017688. MR acknowledges the careful proofreading of the manuscript by Maria Kawula.

REFERENCES

1. Moskal P, Stępień EŁ. Prospects and Clinical Perspectives of Total-Body PET Imaging Using Plastic Scintillators. PET Clin. 2020 Oct;15(4):439–52. doi: https://doi.org/10.1016/j.cpet.2020.06.009.
2. Moskal P, Kowalski P, Shopa RY, Raczyński L, Baran J, Chug N, et al. Simulating NEMA characteristics of the modular total-body J-PET scanner – an economic total-body PET from plastic scintillators. Phys. Med. Biol. 2021;66:175015.
3. Dadgar M, Parzych S, Ardebili FT, Baran J, Chug N, Curceanu C, et al. Investigation of novel preclinical Total Body PET designed with J-PET technology: A simu-lation study. IEEE Transactions on Radiation and Plasma Medical Sciences. 2023 Feb;7(2):124–31. doi: https://doi.org/10.1109/TRPMS.2022.3211780.
4. Baran J, Krzemien W, Parzych S, Raczyński L, Bała M, Coussat A, et al. Realistic total-body J-PET geometry optimization: Monte Carlo study. Med. Phys. 2025;52:2961.
5. Vandenberghe S, Moskal P, Karp J. State of the art in total body PET. EJNMMI Phys. 2020 May 25;7(1):35. doi: https://doi.org/10.1186/s40658-020-00290-2.
6. Badawi RD, Shi H, Hu P, Chen S, Xu T, Price PM, et al. First Human Imaging Studies with the EXPLORER Total-Body PET Scanner. J Nucl Med. 2019 Mar;60(3):299–303. doi: https://doi.org/10.2967/jnumed.119.226498.
7. Spencer BA, Berg E, Schmall JP, Omidvari N, Leung EK, Abdelhafez YG, et al. Performance Evaluation of the uEXPLORER Total-Body PET/CT Scanner Based on NEMA NU 2-2018 with Additional Tests to Characterize PET Scanners with a Long Axial Field of View. J Nucl Med. 2021 Jun 1;62(6):861–70. doi: https://doi.org/10.2967/jnumed.120.250597.
8. Prenosil GA, Sari H, Fürstner M, Afshar-Oromieh A, Shi K, Rominger A, et al. Performance Characteristics of the Biograph Vision Quadra PET/CT System with a Long Axial Field of View Using the NEMA NU 2-2018 Standard. J. Nucl. Med. 2022 Mar;63(3):476–84.
9. Zhang H, Ren C, Liu Y, Yan X, Liu M, Hao Z, et al. Performance Characteristics of a New Generation 148-cm Axial Field-of-View uMI Panorama GS PET/CT System with Extended NEMA NU 2-2018 and EARL Standards. J Nucl Med. 2024 Dec;65(12):1974–82.
10. Moskal P. Positronium Imaging. In: 2019 IEEE Nuclear Science Symposium and Medical Imaging Conference (NSS/MIC); 26 Oct–2 Nov 2019; Manchester, United Kingdom. IEEE; 2019. p. 1–3. https://doi.org/10.1109/nss/mic42101.2019.9059856.
11. Moskal P, Baran J, Bass S, Choiński J, Chug N, Curceanu C, et al. Positronium image of the human brain in vivo. Sci Adv. 2024;10:eadp2840.
12. Bass SD, Mariazzi S, Moskal P, Stępień E. Colloquium: Positronium physics and biomedical applications. Rev. Mod. Phys. 2023;95:021002.
13. Moskal P, Kumar D, Sharma S, Beyene EY, Chug N, Coussat A, et al. Non-maximal entanglement of photons from positron-electron annihilation demonstrated using a plastic PET scanner. Sci Adv. 2025;11:eads3046.
14. Moskal P, Niedźwiecki S, Bednarski T, Czerwiński E, Kapłon Ł, Kubicz E, et al. Test of a single module of the J-PET scanner based on plastic scintillators. Nucl Instrum Methods Phys Res Sect A. 2014;764:317.
15. Niedzwiecki S, Bialas P, Curceanu C, Czerwinski E, Dulski K, Gajos A, Glowacz B, et al. J-PET: a new technology for the whole-body PET imaging. Acta Physica Polonica B. 2017;48:1567.
16. Moskal P, Gajos A, Mohammed M, Chhokar J, Chug N, Curceanu C et al. Testing CPT symmetry in ortho-positronium decays with positronium annihilation tomography. Nat. Commun. 2021;12:5658.

17. Tayefi Ardebili F, Moskal P. Assessing the Spatial Resolution of the Modular J-PET Scanner using the Maximum-Likelihood Expectation-Maximization (MLEM) algorithm. Bio-Algorithms and Med-Systems. 2024; 20(Special Issue):1–9. https://doi.org/10.5604/01.3001.0054.8095.

18. Moskal P, Stępień E, Khreptak A. A vision to increase the availability of PET diagnostics in low- and medium-income countries by combining a low-cost modular J-PET tomograph with the 44Ti/44Sc generator. Bio--Algorithms and Med-Systems. 2024;20(Special Issue):55–62. https://doi.org/10.5604/01.3001.0054.9273.

19. Paterson LM, Kornum BR, Nutt DJ, Pike VW, Knudsen GM. 5-HT radioligands for human brain imaging with PET and SPECT. Med Res Rev. 2013;33:54.

20. Vijay A, Wang S, Worhunsky P, Zheng MQ, Nabulsi N, Ropchan J, et al. PET imaging reveals sex differences in kappa opioid receptor availability in humans, in vivo. Am J Nucl Med Mol Imaging. 2016 Aug 20;6(4):205–14.

21. Gunn RN, Lammertsma AA, Hume SP, Cunningham VJ. Parametric imaging of ligand-receptor binding in PET using a simplified reference region model. Neuroimage. 1997 Nov;6(4):279–87. doi: https://doi.org/10.1006/nimg.1997.0303.

22. Jack CR Jr, Bennett DA, Blennow K, Carrillo MC, Dunn B, Haeberlein SB, et al. NIA-AA Research Framework: Toward a biological definition of Alzheimer's disease. Alzheimers Dement. 2018 Apr;14(4):535–62. doi: https://doi.org/10.1016/j.jalz.2018.02.018.

23. Galldiks N, Langen KJ, Albert NL, Chamberlain M, Soffietti R, Kim MM, et al. PET imaging in patients with brain metastasis-report of the RANO/PET group. Neuro Oncol. 2019 May 6;21(5):585–95. doi: https://doi.org/10.1093/neuonc/noz003.

24. Gonzalez-Montoro A, Barbera J, Sanchez D, Mondejar A, Freire M, Diaz K, et al. A new brain dedicated PET scanner with 4D detector information. Bio-Algorithms and Med-Systems. 2022;18(1):107–19. https://doi.org/10.2478/bioal-2022-0083.

25. Akamatsu G, Takahashi M, Tashima H, Iwao Y, Yoshida E, Wakizaka H, et al. Performance evaluation of VRAIN: a brain-dedicated PET with a hemispherical detector arrangement. Phys Med Amp Biol. 2022;67:225011.

26. Volpi T, Toyonaga T, Khattar N, Gallezot J-D, Naganawa M, Vanderlinden G, et al. Exceptional brain PET images from the NeuroEXPLORER: scans with targeted radiopharmaceuticals and comparison to HRRT. Eur J Nucl Med Mol Imaging. 2024;65:1320.

27. Bartlett EA, Lesanpezeshki M, Anishchenko S, Shkolnik I, Ogden RT, Mann JJ, et al. Dynamic Human Brain Imaging with a Portable PET Camera: Comparison to a Standard Scanner. J Nucl Med. 2024 Feb 1;65(2):320–6. doi: https://doi.org/10.2967/jnumed.122.265309.

28. Wang Z, Cao X, LaBella A, Zeng X, Biegon A, Franceschi D, et al. High-resolution and high-sensitivity PET for quantitative molecular imaging of the monoaminergic nuclei: A GATE simulation study. Med Phys. 2022;49:4430–44.

29. Layden C, Klein K, Matava W, Sadam A, Abouzahr F, Proga M, et al. Design and modeling of a high resolution and high sensitivity PET brain scanner with double-ended readout. Biomed Phys Amp Eng Express. 2022;8:025011.

30. Onishi Y, Isobe T, Ito M, Hashimoto F, Omura T, Yoshikawa E. Performance evaluation of dedicated brain PET scanner with motion correction system. Ann Nucl Med. 2022;36:746.

31. Morimoto-Ishikawa D, Hanaoka K, Watanabe S, Yamada T, Yamakawa Y, Minagawa S, et al. Evaluation of the performance of a high-resolution time-of-flight PET system dedicated to the head and breast according to NEMA NU 2-2012 standard. EJNMMI Phys. 2022 Dec 16;9(1):88. doi: https://doi.org/10.1186/s40658-022-00518-3.

32. Cabrera-Martín MN, González-Pavón G, Hernández MS, Morera-Ballester C, Matías-Guiu JA, Delgado JLC. Validation technique and improvements introduced in a new dedicated brain positron emission tomograph (CareMiBrain). Revista Española de Medicina Nuclear e Imagen Molecular (English Edition). 2021;40:239.

33. Tao W, Weng F, Chen G, Lv L, Zhao Z, Xie S, et al. Design study of fully wearable high-performance brain PETs for neuroimaging in free movement. Phys. Med. Biol. 2020;65:229502.

34. Xu J, Zhao Z, Xie S, Shi D, Huang Q, Peng Q. Mind-Tracker PET: A wearable PET camera for brain imaging. W: 2017 IEEE Nuclear Science Symposium and Medical Imaging Conference (NSS/MIC) [Internet]; 21–28 Oct 2017; Atlanta, GA. IEEE; 2017. p. 1–2. https://doi.org/10.1109/nssmic.2017.8532744.

35. Catana C. Development of Dedicated Brain PET Imaging Devices: Recent Advances and Future Perspectives. J Nucl Med. 2019 Aug;60(8):1044–52. doi: https://doi.org/10.2967/jnumed.118.217901.

36. Majewski S. Imaging is believing: The future of human total-body molecular imaging starts now. Il nuovo cimento C. 2020;43:1.

37. Majewski S. Perspectives of brain imaging with PET systems. Bio-Algorithms and Med-Systems. 2021;17:269–91.

38. Allen MS, Scipioni M, Catana C. New Horizons in Brain PET Instrumentation. PET Clin. 2024 Jan;19(1):25–36. doi: https://doi.org/10.1016/j.cpet.2023.08.001.

39. Rädler M. Simulation studies of a brain pet insert for the total body j-pet tomograph, Presented at the 5th Jagiellonian Symposium on Advances in Particle Physics and Medicine (2024), Kraków, Poland, July 2024.

40. Reddin JS, Scheuermann JS, Bharkhada D, Smith AM, Casey ME, Conti M, et al. Performance Evaluation of the SiPM-based Siemens Biograph Vision PET/CT System. In: 2018 IEEE Nuclear Science Symposium and Medical Imaging Conference (NSS/MIC); 10–17 Nov 2018; Sydney, Australia: IEEE; 2018. p. 1–5. https://doi.org/10.1109/nssmic.2018.8824710.

41. Reynés-Llompart G, Gámez-Cenzano C, Romero-Zayas I, Rodríguez--Bel L, Vercher-Conejero JL, Martí-Climent JM. Phantom, clinical and texture indices evaluation and optimization of a Penalized-Likelihood Image Reconstruction Method (Q.Clear) on a BGO PET/CT scanner. J Nucl Med. 2017;58:1155.

42. Yamagishi S, Miwa K, Kamitaki S, Anraku K, Sato S, Yamao T, et al. Performance Characteristics of a New-Generation Digital Bismuth Germanium Oxide PET/CT System, Omni Legend 32, According to NEMA NU 2-2018 Standards. J Nucl Med. 2023 Dec 1;64(12):1990–7. doi: https://doi.org/10.2967/jnumed.123.266140.

43. Rausch I, Ruiz A, Valverde-Pascual I, Cal-González J, Beyer T, Carrio I. Performance Evaluation of the Vereos PET/CT System According to the NEMA NU2-2012 Standard. J Nucl Med. 2019 Apr;60(4):561–7. doi: https://doi.org/10.2967/jnumed.118.215541.

44. Teräs M, Tolvanen T, Johansson JJ, Williams JJ, Knuuti J. Performance of the new generation of whole-body PET/CT scanners: Discovery STE and Discovery VCT. Eur J Nucl Med Mol Imaging. 2007;34:1683.

45. Aykac M, Bal H, Panin V, Conti M. A study of narrow energy window on the siemens vision 600 pet/ct scanner. J Nucl Med. 2020;61(suppl 1):390.

46. Parzych S. Optimization of positronium imaging performance of a simulated modular J-PET scanner using GATE software. Bio-Algorithms and Med-Systems. 2023;19(1):80–6. https://doi.org/10.5604/01.3001.0054.1937.

47. Kowalski P, Wiślicki W, Shopa RY, Raczyński L, Klimaszewski K, Curcenau C, et al. Estimating the NEMA characteristics of the J-PET tomograph using the GATE package. Phys. Med. Biol. 2018;63(16):165008. doi: https://doi.org/10.1088/1361-6560/aad29b.

48. Raczyński L, Wiślicki W, Krzemień W, Kowalski P, Alfs D, Bednarski T, et al. Calculation of the time resolution of the J-PET tomograph using kernel density estimation. Phys. Med. Biol. 2017;62:5076.

49. Kowalski P, Wiślicki W, Raczyński L, Alfs D, Bednarski T, Białas P, et al. Scatter Fraction Of The J-PET Tomography Scanner. Acta Phys. Pol. B. 2016;47:549.

50. Moskal P, Bednarski T, Białas P, Ciszewska M, Czerwiński E, Heczko A, et al. Strip-PET: A novel detector concept for the TOF-PET scanner. Nucl. Med. Rev. 2012;15(C):C68–C69.

51. Moskal P, Rundel O, Alfs D, Bednarski T, Białas P, Czerwiński E, et al. A Time resolution of the plastic scintillator strips with matrix photomultiplier readout for J-PET tomograph. Phys. Med. Biol. 2016;61:2025.

52. Tayefi Ardebili K, Niedźwiecki S, Moskal P, on behalf of J-PET collaboration. SiPM Performance Characterization for Total-Body J-PET: Hamamatsu vs. Onsemi. 2nd Symposium on new trends in nuclear and medical physics; [cited 2025 Sept 5]. Available from: https://indico.koza.if.uj.edu.pl/event/18/contributions/1698/.

53. Jan S, Santin G, Strul D, Staelens S, Assié K, Autret D, et al. GATE: a simulation toolkit for PET and SPECT. Phys Med Biol. 2004 Oct 7;49(19):4543–61. doi: https://doi.org/10.1088/0031-9155/49/19/007.

54. Jan S, Benoit D, Becheva E, Carlier T, Cassol F, Descourt P, et al. GATE V6: a major enhancement of the GATE simulation platform enabling modelling of CT and radiotherapy. Phys. Med. Biol. 2011;56:881.

55. Sarrut D, Bardiès M, Boussion N, Freud N, Jan S, Létang J-M, et al. A review of the use and potential of the GATE Monte Carlo simulation code for radiation therapy and dosimetry applications. Med Phys. 2014;41:064301.

56. Sarrut D, Bała M, Bardiès M, Bert J, Chauvin M, Chatzipapas K, et al. Advanced Monte Carlo simulations of emission tomography imaging systems with GATE. Phys Med Biol. 2021 May 14;66(10):10.1088/1361--6560/abf276. doi: https://doi.org/10.1088/1361-6560/abf276.

57. Sarrut D, Baudier T, Borys D, Etxebeste A, Fuchs H, Gajewski J, et al. The opengate ecosystem for monte carlo simulation in medical physics. Phys Med Biol. 2022;67(18):184001.

58. Kochebina O, Bonifacio DA, Konstantinou G, Paillet A, Pommranz CM, Razdevšek G, Sharyy V, Yvon D, Jan S. New GATE Digitizer Unit for versions post v9.3. Front Phys. 2024;12:1294916.

59. Tayefi Ardebili K, Niedzwiecki S, Moskal P. Development of a Cost-Effective Total Body J-PET from Plastic Scintillators: Definitive Design. PSMR2024 10th Conference on PET, SPECT, and MR Multimodal Technologies, Total Body and Fast Timing in Medical Imaging; [cited 2025 Sept 5]. Available from: https://agenda.infn.it/event/36860/contributions/230099/contribution.pdf.

60. Smyrski J, Alfs D, Bednarski T, Białas P, Czerwiński E, Dulski K, et al. Measurement of gamma quantum interaction point in plastic scintillator with WLS strips. Nucl. Instrum. Methods Phys. Res. A. 2017;851:39.

61. Gordon CC, Blackwell CL, Bradtmiller B, Parham JL, Barrientos P, Paquette SP, et al. 2012 Anthropometric Survey of U.S. Army Personnel: Methods and Summary Statistics, Tech. Rep. TR-15/007 (U.S. Army Natick Soldier Research, Development and Engineering Center, Natick, MA, 2014).

62. opengate.readthedocs.io [Internet]. Variables printed in monospace use the GATE naming convention; [cited 2025 Sept 5]. Available from: https://opengate.readthedocs.io/en/latest/.

63. IN2P3 Events Directory (Indico) [Internet]. Rädler M, Moskal P, on behalf of the J-PET collaboration. GATE simulations of a multi-detector geometry: combining the total body J-PET with a brain insert. Presented at the GATE Scientific meeting in Athens, Greece; [cited 2025 Sept 5]. Available from: https://indico.in2p3.fr/event/35555/contributions/152184/.